Decoding 122-type iron-based superconductors: A comprehensive simulation of phase diagrams and transition temperatures

Chi Ho Wong [1,2,*] and Rolf Lortz[1,†]

[1]*Department of Physics, The Hong Kong University of Science and Technology, Hong Kong 999077*
[2]*Department of Industrial and Systems Engineering, The Hong Kong Polytechnic University, Hong Kong 999077*

Iron-based superconductors, a cornerstone of low-temperature physics, have been the subject of numerous theoretical models aimed at deciphering their complex behavior. In this study, we present a comprehensive approach that amalgamates several existing models and incorporates experimental data to simulate the superconducting phase diagrams of the principal "122-type" iron-based compounds. Our model considers a multitude of factors including the momentum dependence of the superconducting gap, spin-orbital coupling, antiferromagnetism, spin-density wave, induced *XY* potential on the tetrahedral structure, and electron-phonon coupling. We have refined the electron-phonon scattering matrix using experimental angle-resolved photoemission spectroscopy data, ensuring that relevant electrons pertinent to iron-based superconductivity are accounted for. This innovative approach allows us to calculate theoretical critical temperature (T_c) values for $Ba_{1-x}K_xFe_2As_2$, $CaFe_2As_2$, and $SrFe_2As_2$ as functions of pressure. These calculated values exhibit remarkable agreement with experimental findings. Furthermore, our model predicts that $MgFe_2As_2$ remains nonsuperconducting irrespective of the applied pressure. Given that 122-type superconductivity at low pressure or low doping concentration has been experimentally validated, our work serves as a powerful predictive tool for generating superconducting phase diagrams at high pressure empirically. This study underscores that the high transition temperatures and the precise doping and pressure dependence of iron-based superconductors are intrinsically linked to an intertwined mechanism involving a strong interplay between structural, magnetic, and electronic degrees of freedom.

I. INTRODUCTION

The 122-type iron-based superconductors (IBSCs), represented by AFe_2As_2 (where A is Ba, Sr, or Ca), has been the subject of extensive study. $BaFe_2As_2$, under ambient pressure, exhibits a stripe-type antiferromagnetic spin-density wave (SDW) order without superconductivity. However, the introduction of external pressure, internal chemical pressure (e.g., isovalent doping [1,2]), or ionic substitution in systems such as $Ba_{1-x}K_xFe_2As_2$ can induce superconductivity [3,4]. The SDW transition is accompanied by a structural change from a tetragonal high-temperature to an orthorhombic low-temperature structure [5], known as a nematic transition. Hole-doped Ba122 presents a rich phase diagram, including a reentrant tetragonal C_4 phase region that restores the fourfold symmetry in the basal plane. This phase is characterized by spin rearrangement [6,7] and somewhat suppresses the superconducting transition [7,8]. $SrFe_2As_2$ and $CaFe_2As_2$ also exhibit IBSCs under pressure [9,10]. Interestingly, $MgFe_2As_2$ does not exhibit superconductivity

despite magnesium's position in the second column of the periodic table [5]. This anomaly underscores the complex interplay between structural, magnetic, and electronic degrees of freedom in these materials. The coexistence of superconductivity with a momentum-dependent superconducting gap with other electronically ordered phases such as antiferromagnetic SDW and nematicity [11], and the presence of strong spin-orbit coupling further highlights the complex unconventional nature of IBSCs.

While it is widely accepted that antiferromagnetism enhances electron-phonon coupling on the Fermi surface in unconventional superconductors, recent studies suggest that the significance of electron-phonon coupling in IBSCs may have been underestimated. Li *et al.* [12] demonstrated that phonon softening in FeAs compounds amplifies electron-phonon coupling by $\sim$1.6. Deng *et al.* [13] interpreted out-of-plane lattice vibrations as a phonon-softening phenomenon, which they incorporated into their calculations to enhance electron-phonon scattering. Coh *et al.* further refined these models and proposed that the electron-phonon scattering matrix in iron-based superconductors was underestimated by a factor of approximately 4 [14]. They attributed this underestimation to the noncancellable nearest-neighbor interactions under an antiferromagnetic SDW, in which the conservation of antiferromagnetic (AFM) energy gives a first amplification factor of 2, and the vertical displacement of lattice Fe caused charge transfer to induce *XY* potential in tetrahedral regions under an antiferromagnetic SDW situation, leading to another factor of 2.2 increase in the electron-phonon scattering matrix

*chkhwong@ust.hk
†lortz@ust.hk

[14]. Wu *et al.* [15] also observed a significant increase in intensity for this abnormal As phonon mode.

Moreover, a discernible shift of the spectral weight between the normal and the superconducting state is evident in the photoemission spectra below the superconducting energy gap of various IBSCs in an energy range of $\sim$30–60 meV below the Fermi energy [16–19]. This shift, observed in the ARPES range, suggests that the involvement of superconducting electrons in IBSCs may have been underestimated. This underestimation could potentially account for the discrepancy between theoretical and experimental T_c values based on the electron-phonon coupling method. Given the high T_c of IBSCs, it is crucial to consider the full electronic density of states (DOS) in a range of $E_F - E_{\text{Debye}}$ to E_F and not only the Fermi level value, where E_{Debye} represents the upper limit of the phonon energies that can be transferred to electrons. This approach, which is a direct consequence of energy conservation, is corroborated by ARPES experiments [16–19] where the energy range of the spectral weight shift is approximately in the order of the Debye energy.

In our quest to decode the intricate electronic phenomena in 122-type IBSCs, we initially turn our attention to $Ba_{1-x}K_xFe_2As_2$ owing to its rich phase diagram [20–23]. Our investigation will delve into and compare the influence of both first-order and higher-order antiferromagnetic fluctuations on the T_c calculations. This comparative analysis will encompass the compounds $Ba_{1-x}K_xFe_2As_2$, $CaFe_2As_2$, and $SrFe_2As_2$. Furthermore, we will explore whether the application of pressure could potentially induce superconductivity in $MgFe_2As_2$. This comprehensive approach aims to shed light on the complex interplay of factors governing superconductivity in these materials.

II. COMPUTATIONAL ALGORITHM

Our T_c calculations include at least six components.

(1) Exchange factor: The pressure dependence of the antiferromagnetic interaction is monitored by the Ising expression. We define M_{Fe} and E_{co} as the Fe moment and the exchange-correlation energy, respectively. The exchange factor becomes $f(E_{ex}) \sim \frac{[M_{\text{Fe}} M_{\text{Fe}} E_{co}]_{P>0}}{[M_{\text{Fe}} M_{\text{Fe}} E_{co}]_{P=0}}$ if pressure P exists.

(2) Coh factor [14]: Antiferromagnetism usually increases the electron-phonon scattering matrix by a ratio of R_{AF} when the *ab initio* calculations change from spin-restricted to spin-unrestricted mode. To encounter the SDW, Coh *et al.* [14] have proposed that the antiferromagnetic SDW background with the induced XY potential (triggered by an abnormal out-of-plane phonon state R_{tetra}) in the tetrahedral region increases the scattering matrix by $R_{\text{Coh}} = R_{SDW} R_{\text{tetra}} \sim 4$, where $R_{SDW} = 2$ and $R_{\text{tetra}} = 2.2$. SDW redistributes the AFM fluctuations which can be interpreted as, at time t, the antifer-

romagnetic fluctuation reaches its maximum at lattice points $(i, i+2, \ldots)$ and its minimum at lattice points $(i+1, i+3, \ldots)$. At time $t\prime = t + dt$, the situation is reversed, with the maximum occurring at lattice points $(+1, i+3, \ldots)$ and the minimum at lattice points $(i, i+2, \ldots)$. This redistribution continues over time but only one iron atom per repeating unit contributes to the scattering matrix and hence the effect is doubled [14]. Whenever there is an energy transfer from AFM fluctuations to electron-phonon coupling, the maximum AFM fluctuation between two neighboring atoms can only combine their own AFM terms in a repeating unit (i.e., $\delta E_{AFM} \rightarrow 2\delta E_{AFM}|_{\text{max}}$), but it turns out that the electron-phonon interaction λ is increased by a factor of 4 (i.e., $\lambda \rightarrow 4\lambda$), indicating a sign of a higher-order AFM fluctuation ($\lambda \propto \delta E_{AFM}^2$). Using the Coh factor brings the simulation results more in line with the experimental observations [24]. However, the appearance of the induced XY potential requires calibrating the GGA+A functional, which is a time-consuming experimental effort and a computationally expensive mission [14,24]. Hence, we define $R_{\text{tetra}} \sim \frac{0.5(DOS_{\text{upper}}^{XY} + DOS_{\text{lower}}^{XY})}{DOS_{\text{both}}^{XY}}$ within the ARPES range [25]. DOS_{upper}^{XY} represents the average electronic density of states for the structure containing only the upper tetrahedral plane, while DOS_{lower}^{XY} indicates the average electronic DOS for the structure that only contains lower tetrahedral planes. DOS_{both}^{XY} is the average electronic DOS representing the original structure coexisting upper and lower tetrahedral regions.

(3) ARPES factor: To include all relevant electrons in IBSC calculations, the average electron-phonon scattering matrix $g_{pp'}(E)$ within the ARPES range [16–19] is $\langle \sum_{E_F - E_{\text{Debye}}}^{E_F} \frac{g_{pp'}(E')}{\varepsilon'} \rangle$. The dielectric constant ε' controls the screening effect when the electrons interact with lattices under the induced XY potential. Including the ARPES factor increases the electron-phonon scattering matrix by $R_{ARPES} \sim \frac{\langle \sum_{E_F - E_{\text{Debye}}}^{E_F} g_{pp'}(E')/\varepsilon' \rangle}{g_{pp'}(E_F)/\varepsilon}$.

(4) Anisotropic factor: The ellipse equation, $p_{\text{angular}}(\theta) = \frac{a_{\text{major}} b_{\text{minor}}}{\sqrt{(b_{\text{minor}}^2 - a_{\text{major}}^2)\cos^2\theta + a_{\text{major}}^2}}$, is used to mimic the effect of an anisotropic momentum space when there is fourfold symmetry [e.g., the two overlapping red ellipses in Fig. 1(a)]. The major a and minor b axes control the area of the k space, $\sim 8 \int_0^{\pi/4} \frac{1}{2} p_{\text{angular}}(\theta)^2 d\theta$, for fourfold symmetry. The anisotropic pairing strength divided by isotropic pairing strength gives $\langle f_{\text{angular}} \rangle$.

(5) Spin-orbital coupling (SOC) factor: The SO coupling of IBSCs [26] is in a few meV. The effect of SOC should be included in the T_c calculation.

(6) Electron-phonon factor: The electron-phonon coupling is $\lambda_{PS} = 2 \int \alpha_{PS}^2 \frac{F(\omega)}{\omega} d\omega$ where $F(\omega)$ is the phonon density of states as a function of frequency ω. Taking into account the above factors, the $\alpha_{PS}^2 F(\omega)$ becomes [27]

$$\alpha_{PS}^2 F(\omega) \sim \left\langle \sum_{V_F - V_{\text{Debye}}}^{V_F} \int \frac{d^2 p_E}{v_E} \right\rangle \left\langle \sum_{V_F - V_{\text{Debye}}}^{V_F} \int \frac{d^2 p'_E}{(2\pi\hbar)^3 v'_E} \right\rangle \sum_v \delta(\omega - \omega_{p-p'v})$$

$$\times \left| \sqrt{\frac{\hbar}{A\omega_{p-p'v}}} \int u_i \nabla(V_{XY} R_{ph}) \psi_p^* R_{SDW} R_{AF} R_{ARPES} \psi_{p'} dr \right|^2 \Bigg/ \left\langle \sum_{V_F - V_{\text{Debye}}}^{V_F} \int \frac{d^2 p_E}{v_E} \right\rangle$$
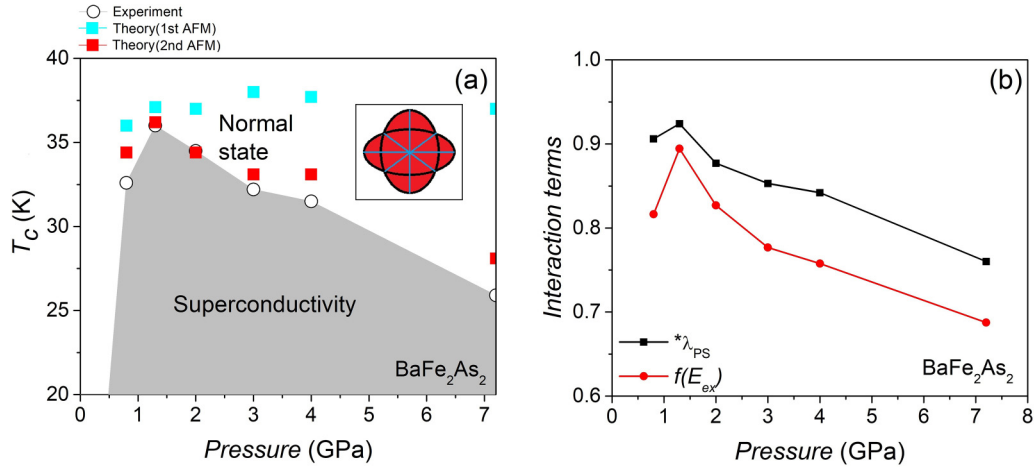
FIG. 1. (a) The T_c distribution [20] and (b) the interaction terms of $BaFe_2As_2$ vs pressure. Instead of using the isotropic $\int 2\pi p\,dp$ in k space, the fourfold symmetry is outlined by two overlapped red ellipses. The blue lines split it into eight regions in equal partition with the subarea of $\int_0^{\pi/4} \frac{1}{2} p_{angular}(\theta)^2 d\theta$.

where $v_E \in (v_F - v_{Debye}, v_F)$ is the velocity in the ARPES range and v_F is the Fermi velocity. The velocity v_{Debye} can be interpreted from the Debye energy. A is a material constant. $\hbar$ is the Planck constant over 2π and $\psi_{p'}$ is the wave function of the electrons. The $\alpha_{PS}^2 F(\omega)$ may be further reduced to $\alpha_{E_F}^2 F(\omega) R_{AF}^2 R_{SDW}^2 R_{tetra}^2 R_{APRES}^2$. In strong-coupling regime, the pairing strength and the Coulomb pseudopotential are renormalized [27] to $^*\lambda_{PS}$ and $^*\mu$. The *ab initio* [28] setup and lattice parameters are listed in the Supplemental Material [29]. The increase in λ resulting from the exchange enhancement can be represented as a separable variable [30]. The separable variable representing the increase in λ due to exchange enhancement, can be obtained by multiplying the pairing strength by the exchange enhancement factor [30]. It should be noted that this is not restricted to the first-order exchange interaction [30]. The parameters influencing antiferromagnetism (AF) under pressure can be described by $R_{AF}^2|_{P>0} \sim R_{AF}^2|_{P=0} f(E_{ex})^2$ and $R_{tetra}^2|_{P>0} \sim R_{tetra}^2|_{P=0} f(E_{ex})^2$ under the second AFM fluctuation. Similarly, we set $R_{AF}^2|_{P>0} \sim R_{AF}^2|_{P=0} f(E_{ex})$ and

$R_{tetra}^2|_{P>0} \sim R_{tetra}^2|_{P=0} f(E_{ex})$ under the first AFM fluctuation. The pairing strength is then substituted into the McMillian T_c formula [27].

III. RESULTS

Figure 1(a) displays our theoretical T_c of $BaFe_2As_2$ under pressure compared to experimental literature data [20]. Our combined model based on the second AFM fluctuation shows a reasonable accuracy in the phase diagram simulation. The pairing strength under the second AFM fluctuation and the exchange factor are optimized at 1.3 GPa, but they are drastically reduced at higher pressures, as shown in Fig. 1(b). The Debye temperatures of uncompressed $BaFe_2As_2$ at the low- and high-temperature limits are 379 and 470 K, respectively [31]. Our computed electron-phonon coupling of $BaFe_2As_2$ at 0.8 GPa only increases from $\lambda_{E_F} = 0.33$ to $\lambda_{E_F(SO)} = 0.37$ after activation of the SOC. However, the Coh and ARPES factors are the main ingredients to increase the pairing strength to ~0.9, allowing the theoretical T_c to occur above ~30 K. The
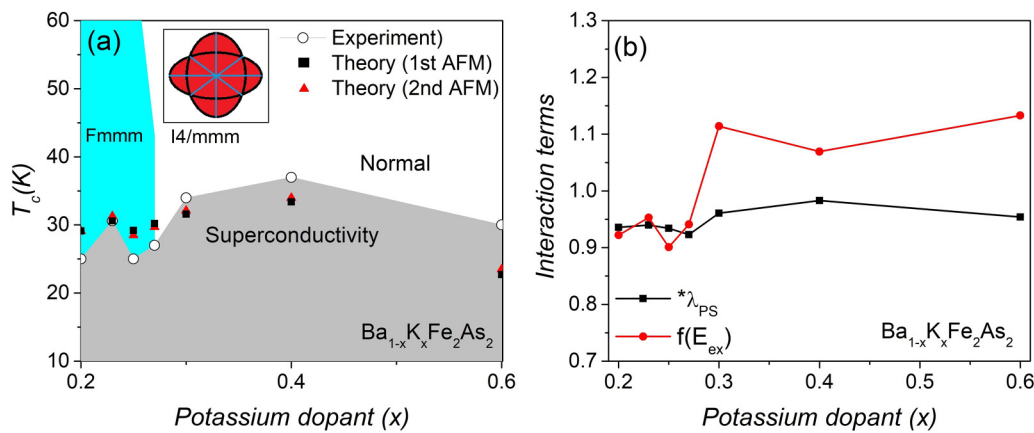

FIG. 2. (a) The doping dependence of the theoretical and experimental [8,32] T_c of $Ba_{1-x}K_xFe_2As_2$. The theoretical and experimental T_c are shown. (b) The individual interaction terms of $Ba_{1-x}K_xFe_2As_2$ as a function of K content. The $^*\lambda_{PS}$ is calculated under second AFM fluctuations.

TABLE I. Comparison between experimental [9,10,34,35] and theoretical T_c of SrFe$_2$As$_2$ and CaFe$_2$As$_2$ under compression.

	Experimental T_c (K)	Theoretical T_c (second AFM) (K)	Theoretical T_c (first AFM) (K)
SrFe$_2$As$_2$ (3 GPa)	30	28.3	30.2
SrFe$_2$As$_2$ (5 GPa)	19	23.5	29.4
CaFe$_2$As$_2$ (0.1 GPa)	12–15	14.6	14.6
CaFe$_2$As$_2$ (1.2 GPa)	12–15	15.1	14.9

decrease in the dielectric constant [30] in the presence of AFM and SDW, and the increase in the effective DOS trigger an increase in the ARPES factor. In contrast, the combined model makes use of the first AFM fluctuation results in a significant discrepancy between the calculated and experimental T_c at high pressures.

The experimental and theoretical T_c values of Ba$_{1-x}$K$_x$Fe$_2$As$_2$ are in close but not perfect agreement, as shown in Fig. 2(a) [8]. The inclusion of either the first or second AFM fluctuation does not have a significant effect on the calculated T_c of Ba$_{1-x}$K$_x$Fe$_2$As$_2$. We import the full set of lattice parameters measured by Rotter *et al.* as a function of doping [32]. In the range of $0.25 < x < 0.27$, the Fe moments are aligned in the out-of-plane direction [8], leading us to set a fixed orientation of the Fe moment in the out-of-plane direction in the *ab initio* simulation. If the fixed orientation of the out-of-plane Fe moment is not considered, the theoretical T_c could be around 32 K. However, due to the out-of-plane Fe moment causing a 15% reduction in the exchange factor, the theoretical T_c values are ultimately reduced by ∼4 K. The Ba$_{0.6}$K$_{0.4}$Fe$_2$As$_2$ has a highest theoretical T_c of ∼34 K. Figure 2(b) illustrates the individual components of the pairing strength. The $^*\lambda_{PS}$ reaches a maximum at $x \sim 0.4$, where our computed value of s-wave λ_{E_F} is 0.88 and the literature value is 0.9 [33]. λ_{E_F} with and without the gap isotropy are 0.77 and 0.88, respectively, which gives $\langle f_{\text{angular}} \rangle = 0.77/0.88 = 0.87$. After the doping concentration is increased from 0.4 to 0.6, the $^*\lambda_{PS}$ decreases slightly.

The T_c calculation based on the second AFM fluctuation of the Ba$_{1-x}$K$_x$Fe$_2$As$_2$ at $x = 0.4$ is demonstrated. Dopants generate a chemical pressure that causes $f(E_{ex}) \sim \frac{[M_{\text{Fe}}^2 E_{co}]_{P>0}}{[M_{\text{Fe}}^2 E_{co}]_{P=0}} = (\frac{1.48^2}{1.41^2})1.027 = 1.132$ (the Fe moments are scaled to the Bohr magneton). The calculated λ_{E_F} (fourfold), $R_{AF}|_{P>0}$, R_{SDW}, $R_{\text{tetra}}|_{P>0}$, and R_{ARPES} are 0.77, 1.18, 2, 1.68, and 2.06, respectively. The pairing strength is

$$^*\lambda_{PS} = \frac{\lambda_{PS}}{\lambda_{PS}+1} = \frac{0.77 \times 1.18^2 \times 2^2 \times 1.68^2 \times 2.06^2}{0.77 \times 1.18^2 \times 2^2 \times 1.68^2 \times 2.06^2 + 1}$$

$$= 0.982$$

TABLE II. Magnetic analysis of MgFe$_2$As$_2$ under pressure.

P (GPa)	Fe moment (μ_B)	P (GPa)	Fe moment (μ_B)
0	0.5	6	0.000
3	0.0	9	0.000

and $^*\mu = \frac{\mu}{\lambda_{PS}+1} = \frac{0.15}{1+0.77 \times 1.18^2 \times 2^2 \times 1.68^2 \times 2.06^2} = 0.0025$.

Substituting the pairing strength into the McMillian T_c formula,

$$T_c = \frac{T_D}{1.45} \exp\left(\frac{-1.04(1+\lambda)}{\lambda - \mu(1+0.62\lambda)}\right)$$

$$= \frac{393}{1.45} \exp\left(\frac{-1.04(1+0.982)}{0.982 - (0.0025)(1+0.62 \times 0.982)}\right)$$

$$= 34.2 \text{ K}.$$

We also estimate the T_c of SrFe$_2$As$_2$ under compression. The theoretical T_c values of SrFe$_2$As$_2$ at low pressures are in good agreement with the experimental data [9] presented in Table I, regardless of whether the first or second AFM fluctuation is used. However, significant discrepancies between the theoretical and experimental T_c values are observed for SrFe$_2$As$_2$ under high-pressure conditions [9]. On the other hand, the theoretical T_c value of CaFe$_2$As$_2$ as a function of pressure the10] does not vary significantly when either the first- or the second-order AFM fluctuation method is used. Furthermore, our calculation reveals that the magnetic moment of MgFe$_2$As$_2$ remains at zero when the pressure exceeds 3 GPa (Table II). We also investigated the relationship between the momentum space and the T_c, as depicted in Fig. 3. It is worth noting that the calculated values of T_c exhibit a minimal change ($\delta T_c \sim 2$–4 K), regardless of the presence of
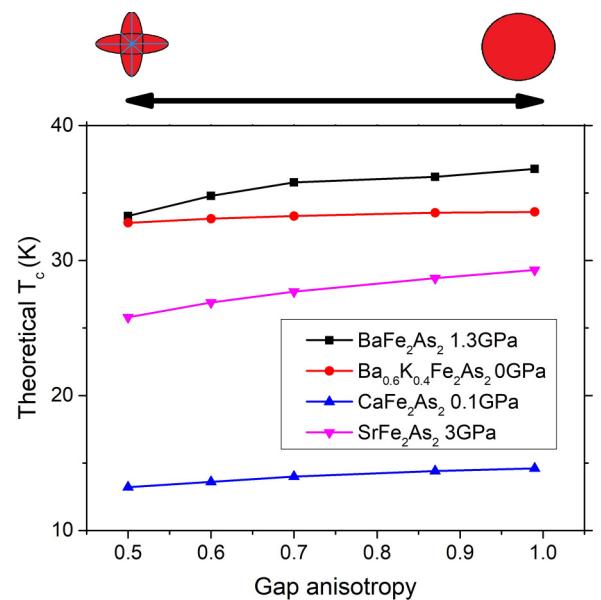
FIG. 3. Effect of the anisotropic factor $\langle f_{\text{angular}} \rangle$ on the theoretical T_c in the studied compounds under the second AFM fluctuation.

gap anisotropy. The theoretical T_c towards an isotropic gap is slightly higher.

IV. DISCUSSION

While our model has demonstrated efficacy in bridging the gap between theoretical and experimental T_c, a comprehensive theory of 122-type IBSCs remains elusive. This paper does not aim to reevaluate the six models outlined in the methodology section, as their scientific validity has been justified in peer-reviewed literature. If a proposed model of IBSCs is deemed incorrect, a universal theory of IBSCs would need to be already in place. However, at present, no universally accepted or fully established unified theory for IBSCs exists. Hence, we refrain from stating whether our model is an important ingredient for the theory of 122-type IBSCs. We do not seek to validate the theory of 122-type IBSCs in this work. Instead, our objective is to amalgamate T_c calculations from these validated studies and systematically integrate each submodel to examine its potential for predicting the phase diagram. Our focus in this section is primarily on data analysis, rather than conjecture about the triggers of 122-type IBSCs.

Our theoretical analysis indicates that considering the first-order AFM fluctuation may not suffice to simulate the complete superconducting phase diagram of BaFe$_2$As$_2$. AFM fluctuations typically diminish under pressure. The pressure-dependent theoretical T_c in BaFe$_2$As$_2$ is significantly improved by using second AFM fluctuation, as the first-order AFM fluctuation does not decrease as rapidly as the second-order AFM fluctuation at high pressures. This aligns with the results of Coh *et al.* [14] where a higher-order AFM fluctuation is employed. Both first- and second-order AFM fluctuations can yield accurate theoretical T_c values at low pressures, as it is feasible to fit a dependent variable (Y) linearly within the high-order term when the independent variable (X) is near zero or small. A similar scenario is observed in SrFe$_2$As$_2$, where only the second-order AFM fluctuations can accurately calculate T_c at high pressure (the exchange factor drops by $\sim$25% rapidly). However, for CaFe$_2$As$_2$, the first-order AFM fluctuation maintains precision in calculating T_c, as its exchange factor only decreases by less than 4% from 0.1 to 1.2 GPa.

Elevating the Debye frequency permits higher energy phonons to interact with a greater number of electrons within the ARPES range [16–19]. This interaction results in an augmentation of the R_{ARPES} value, as the effective electronic DOS increases. However, the $f(E_{ex})$ usually mitigates the impact of R_{AF} and R_{tetra} at high pressures. The implementation of the second-order AFM fluctuation is crucial to decrease the T_c of BaFe$_2$As$_2$ above $\sim$2 GPa. The R_{ARPES} factor accounts for electron energies situated down to $\sim$30 meV below the Fermi level. This method continues to adhere to the hyperbolic tangent shape of the Fermi-Dirac statistics across the Fermi level at a finite temperature [27]. The correlation between T_c and AFM fluctuations, as depicted in Figs. 1(b) and 2(b), underscores the significance of AFM fluctuations in the superconducting pairing process.

Although our theoretical T_c values of Ba$_{1-x}$K$_x$Fe$_2$As$_2$ are not devoid of errors, the T_c profiles depicted in Fig. 2(a)

align more closely with the experimental data. The dopant-induced pressure in Ba$_{1-x}$K$_x$Fe$_2$As$_2$ is relatively weak, hence the combined model based on first-order AFM fluctuation remains accurate. The same pairing strength formulas are applied for BaFe$_2$As$_2$, Ba$_{1-x}$K$_x$Fe$_2$As$_2$, CaFe$_2$As$_2$, SrFe$_2$As$_2$, and MgFe$_2$As$_2$ with reasonably well-calculated T_c, suggesting that the pairing mechanism of these four undoped iron-based superconductors may share similar components from a statistical perspective. No T_c has been reported for MgFe$_2$As$_2$. This may be due to the fact that as the $f(E_{ex})$ drops to zero above 3 GPa, the pairing strength becomes zero and we propose that pressure is not an effective method to induce IBSCs in MgFe$_2$As$_2$.

In certain IBSCs, the Fermi surface displays nematic order, which influences the superconducting order parameter. The precise effect of nematic order or spin-orbital coupling on the pairing symmetry on the Fermi surface is still an open question [36–41]. However, the intricate interactions between electrons on the Fermi surface can be paled by considering all high-energy electrons within the ARPES range. High-energy electrons should not anticipate involving either nematicity or fourfold symmetry in the superconducting gap. Even though we include the fourfold effects on the high-energy electrons, the pairing strength is only weakened by $\sim$20%–30% when transitioning to fourfold or d-wave-like symmetry [42], which validates our calculated value of $\langle f_{angular} \rangle \sim 0.8$ and the change in T_c is only a few kelvin, as depicted in Fig. 3. We have not examined the case of $\langle f_{angular} \rangle \leqslant 0.5$ because reducing the pairing strength by gap anisotropy necessitates the formation of a p-wave order parameter [43], and none of our studied compounds are expected to be p-wave superconductors.

Nematicity may emerge under pressure or doping [44]. However, as evident in FeSe$_{1-y}$S$_y$ [40,41], the T_c across the nematic transition points (e.g., $y \sim 0.18$ at 0 GPa, or $\sim$0.09 at 0.5GPa) show a tiny change only ($\Delta T \sim 1$ K) [40,41], where $\Delta T << T_c$. Upon preliminary observation, the triggers of nematicity in the form of anisotropic gap appear to exert minimal influence on the T_c values, and our simulator supports this experimental evidence in Fig. 3. However, this does not suggest that they are inconsequential to the mechanism of IBSCs. In fact, nematicity, antiferromagnetism, spin-orbital coupling, and spin-density wave play a pivotal role in initiating IBSCs [40], while the pressure dependence of T_c is likely dominated by antiferromagnetism. Once the IBSC is triggered, the impact of the anisotropic factor diminishes due to the renormalization of the strong original pairing strength in compressed IBSCs. Therefore, it would be unfair to assess the significance of the anisotropy factor or nematicity based solely on Fig. 3. A systematic analysis of nematicity will be needed to fine-tune the T_c values in our future work. Since the primary objective of this paper is to create a T_c simulator for the compounds, rather than focusing on validating the theory of IBSCs, the method we have developed demonstrates a reasonable performance.

Another potential source of error in T_c could be the approximation of the Debye energy in the ARPES factor. A trend can be observed between the ARPES range and the Debye energy

when comparing the ARPES data of different materials. An examination of the ARPES data of LiFeAs, FeSe, and FeSe/SrTiO$_3$ provides insights into this observation. In the case of FeSe/SrTiO$_3$, the T_c is approximately 100 K [18], and the interfacial Fuchs-Kliewer (F-K) phonon energy is 1150 K [45] with strong electron-phonon coupling [44]. Concurrently, the ARPES range in this context is measured to be between 0.1 and 0.3 eV [18]. For LiFeAs or FeSe, the T_c is lower [12], around 10 K, and the phonon energy is approximately 300 K (ratio of $T_{\text{Debye}} = 1150K/300K \sim 4$). Correspondingly, the ARPES ranges for LiFeAs and FeSe are much narrower, around 0.03–0.06 eV (ratio of the ARPES range="0.1–0.3 eV"/"0.03–0.06 eV" also equals ~ 4). These data suggest a trend where an increase in Debye energy corresponds to an increase in the ARPES range, indicating a broader energy range for electronic excitations. Therefore, we select the Debye energy as an approximated energy range in the ARPES factor, but it may not precisely correspond to the actual energy range below the Fermi level. This approximation can lead to either an overestimation or underestimation of T_c. To rectify this issue, one could determine the exact ARPES range for each IBSC and use that value instead of an approximation. This approach would yield a more accurate estimation of the ARPES factor. However, scanning all ARPES data for every discovered IBSC would indeed require significant experimental effort and pose practical challenges. Further theoretical work is needed to fine-tune the APRES range in the calculations.

In the ideal case, there would be a universal density functional theory (DFT) functional capable of describing all IBSC phenomena, but the empirical search of the ideal case continues. In the absence of this ideal case, we explore alternative methods. We are keen on relying on reintegrating more analytical components to bring advantages in terms of understanding. The $\lambda_{E_F(SO)}$ and R_{AF} are obtained explicitly from an *ab initio* method rather than taking the values from other IBSC samples empirically. $\langle f_{\text{angular}} \rangle$ is calculated by comparing the pairing strengths under fourfold and s-wave symmetry, using the analytic integral of k space. R_{SDW} can be derived through analytical considerations of AFM energy conservation during the formation of SDW. The effect of R_{tetra} in FeSe is confirmed explicitly through the matrix calculation [14] and experiment [24]. R_{tetra} has been recalculated in the 122-FeAs system instead of substituting the R_{tetra} value of FeSe, which eliminates any doubt about an empirical substitution. With this approach, we can bring back the renowned Ising expression $f(E_{ex})$ to analytically assess the AFM vs pressure, which enhances the comprehension in the field. We used a commercial package to incorporate the effects of antiferromagnetism and spin-orbit coupling on electron-phonon coupling in an integrated manner and meanwhile, during the *ab initio* simulations, the package has automatically generated the shape of the momentum space. Besides, when the differential out-of-plane phonon in the form of charge density wave between the adjacent Fe atoms emerged under antiferromagnetism, we have also observed a major increase in the magnetic moment of a Fe atom per unit cell. However, it is important to note that we did not manually include this increase in the magnetic moment in the exchange factor and

the DFT code. This is because the spin-density wave (R_{SDW}) factor of 2 is already accounted for. We also do not add the effect of the induced electric polarization due to the differential out-of-plane phonon in the DFT code of electron-phonon coupling calculation because the R_{tetra} has already encountered the effect. Therefore, any overestimation of the effects does not occur.

There are two valid approaches to addressing a problem: (1) starting from correlations and investigating how different forms of order can evolve, and (2) identifying existing orders and examining their mutual influences. In our research, we have chosen the second approach. While the first method has provided valuable insights into the intertwined nature of SDW and nematic orders, etc., it has not yet advanced to the subsequent step of offering new insights into understanding the large superconducting gap to substantiate the impact of individual effects. In contrast, our study demonstrates that considering additional orders can contribute to the emergence of high-temperature superconductivity within an expanded electron-phonon coupling framework based on the intertwined nature. Our decision to adopt an amplified electron-phonon coupling framework as the starting point is not without merit. This choice is supported by experimental evidence [18] of a significantly strong electron-phonon coupling in the IBSC T_c record holder (FeSe/SrTiO$_3$). The existence of such a coupling provides a compelling rationale for exploring its potential role in driving the superconducting behavior observed in IBSCs. It is important to note that our intention is not to discredit the first method. Using the first method is important because it has confirmed the nominated factors of triggering IBSCs, but we rather provide an alternative perspective that explores the influence of various orders on the superconducting behavior.

Our model may not be intended for discovering new IBSC compounds. Rather, it may be suitable for predicting T_c at higher pressures or heavy doping levels if superconductivity has already been confirmed at ambient pressure, low pressure, or low doping concentration. Despite bridging the gap between theoretical and experimental T_c values, the combined model does not explicitly provide a definitive statement about the pairing mechanism of IBSCs. The unified theory of iron-based superconductors remains an open question necessitating further investigation and research. The possibility of other models capable of producing accurate theoretical T_c of IBSCs via entirely different mechanisms is not excluded.

Data are sharable under reasonable request. The authors are usually supportive of reproducing the results if assistance is needed (please send requests to [46]).

V. CONCLUSIONS

We have successfully established a framework for simulating the superconducting phase diagrams of major 122-type IBSCs with commendable accuracy. Our observations indicate that certain IBSCs require the consideration of higher-order antiferromagnetic fluctuations, particularly under high-pressure conditions. This is a pivotal step towards integrating various effects into the pairing mechanism of IBSCs,

including gap anisotropy, spin-orbital coupling, high-energy electrons, abnormal phonon behavior, screening effects, spin-density wave, and antiferromagnetism. Our findings pave the way for analyzing the complex interplay of factors governing superconductivity in these materials.

ACKNOWLEDGMENT

[1] S. Sharma, S. Bharathia, S. Chandra, V. R. Reddy, S. Paulraj, A. T. Satya, V. S. Sastry, A. Gupta, and C. S. Sundar, Superconductivity in Ru-substituted polycrystalline $BaFe_{2-x}Ru_xAs_2$, Phys. Rev. B **81**, 174512 (2010).

[2] S. Kasahara, T. Shibauchi, K. Hashimoto, K. Ikada, S. Tonegawa, R. Okazaki, H. Shishido, H. Ikeda, H. Takeya, K. Hirata, T. Terashima, and Y. Matsuda, Evolution from non-Fermi- to Fermi-liquid transport via isovalent doping in $BaFe_2(As_{1-x}P_x)_2$ superconductors, Phys. Rev. B **81**, 184519 (2010).

[3] M. Rotter, M. Tegel, and D. Johrendt, Superconductivity at 38 K in the iron arsenide $(Ba_{1-x}K_x)Fe_2As_2$, Phys. Rev. Lett. **101**, 107006 (2008).

[4] A. S. Sefat, R. Jin, M. A. McGuire, B. C. Sales, D. J. Singh, and D. Mandrus, Superconductivity at 22 K in Co-doped $BaFe_2As_2$ crystals, Phys. Rev. Lett. **101**, 117004 (2008).

[5] J. Paglione and R. L. Greene, High-temperature superconductivity in iron-based materials, Nat. Phys. **6**, 645 (2010).

[6] J. M. Allred, K. M. Taddei, D. E. Bugaris, M. J. Krogstad, S. H. Lapidus, D. Y. Chung, H. Claus, M. G. Kanatzidis, D. E. Brown, J. Kang, R. M. Fernandes, I. Eremin, S. Rosenkranz, O. Chmaissem, and R. Osborn, Double-Q spin-density wave in iron arsenide superconductors, Nat. Phys. **12**, 493 (2016).

[7] J. Hou, C.-w. Cho, J. Shen, P. M. Tam, I-H. Kao, M. H. G. Lee, P. Adelmann, T. Wolf, and R. Lortz, Possible coexistence of double-Q magnetic order and chequerboard charge order in the re-entrant tetragonal phase of $Ba_{0.76}K_{0.24}Fe_2As_2$, Phys. C (Amsterdam, Neth.) **539**, 30 (2017).

[8] A. E. Böhmer, F. Hardy, L. Wang, T. Wolf, P. Schweiss, and C. Meingast, Superconductivity-induced re-entrance of the orthorhombic distortion in $Ba_{1-x}K_xFe_2As_2$, Nat. Commun. **6**, 7911 (2015).

[9] P. L. Alireza, Y. T. C. Ko, J. Gillett, C. M. Petrone, J. M. Cole, G. G. Lonzarich, and S. E. Sebastian, Superconductivity up to 29 K in $SrFe_2As_2$ and $BaFe_2As_2$ at high pressures, J. Phys.: Condens. Matter **21**, 012208 (2009).

[10] Y. Zheng, Y. Wang, B. Lv, C. W. Chu, and R. Lortz, Thermodynamic evidence for pressure-induced bulk superconductivity in the Fe–As pnictide superconductor $CaFe_2As_2$, New J. Phys. **14**, 053034 (2012).

[11] A. E. Böhmer and A. Kreisel, Nematicity, magnetism and superconductivity in FeSe, J. Phys.: Condens. Matter **30**, 023001 (2018).

[12] B. Li, Z. W. Xing, G. Q. Huang, and M. Liu, Magnetic-enhanced electron-phonon coupling and vacancy effect in "111"-type iron pnictides from first-principle calculations, J. Appl. Phys. **111**, 033922 (2012).

[13] S. Deng, J. Köhler, and A. Simon, Electronic structure and lattice dynamics of NaFeAs, Phys. Rev. B **80**, 214508 (2009).

[14] S. Coh, M. L. Cohen, and S. G. Louie, Anti-ferromagnetism enables electron-phonon coupling in iron-based superconductors, Phys. Rev. B **94**, 104505 (2016).

[15] S.-F. Wu, W.-L. Zhang, V. K. Thorsmølle, G. F. Chen, G. T. Tan, P. C. Dai, Y. G. Shi, C. Q. Jin, T. Shibauchi, S. Kasahara, Y. Matsuda, A. S. Sefat, H. Ding, P. Richard, and G. Blumberg, In-plane electronic anisotropy resulted from ordered magnetic moment in iron-based superconductors, Phys. Rev. Res. **2**, 033140 (2020).

[16] J. Xiao-Wen1, L. Hai-Yun, Z. Wen-Tao, Z. Lin, M. Jian-Qiao, L. Guo-Dong, D. Xiao-Li, W. Gang, L. Rong-Hua, C. Xian-Hui *et al.*, Common features in electronic structure of the oxypnictide superconductors from photoemission spectroscopy, Chin. Phys. Lett. **25**, 3765 (2008).

[17] C. Liu, G. D. Samolyuk, Y. Lee, N. Ni, T. Kondo, A. F. Santander-Syro, S. L. Bud'ko, J. L. McChesney, E. Rotenberg, T. Valla, A. V. Fedorov, P. C. Canfield, B. N. Harmon, and A. Kaminski, K-doping dependence of the Fermi surface of the iron-arsenic $Ba_{1-x}K_xFe_2As_2$ superconductor using angle-resolved photoemission spectroscopy, Phys. Rev. Lett. **101**, 177005 (2008).

[18] C. Zhang *et al.*, Ubiquitous strong electron–phonon coupling at the interface of $FeSe/SrTiO_3$, Nat. Commun. **8**, 14468 (2017).

[19] U. Stockert, M. Abdel-Hafiez, D. V. Evtushinsky, V. B. Zabolotnyy, A. U. B. Wolter, S. Wurmehl, I. Morozov, R. Klingeler, S. V. Borisenko, and B. Büchner, Specific heat and angle-resolved photoemission spectroscopy study of the superconducting gaps in LiFeAs, Phys. Rev. B **83**, 224512 (2011).

[20] A. Mani, N. Ghosh, S. Paulraj, A. Bharathi, and C. S. Sundar, Pressure-induced superconductivity in $BaFe_2As_2$ single crystal, Europhys. Lett. **87**, 17004 (2009).

[21] F. Hardy, A. E. Böhmer, D. Aoki, P. Burger, T. Wolf, P. Schweiss, R. Heid, P. Adelmann, Y. X. Yao, G. Kotliar, J. Schmalian, and C. Meingast, Evidence of strong correlations and coherence-incoherence crossover in the iron pnictide superconductor KFe_2As_2, Phys. Rev. Lett. **111**, 027002 (2013).

[22] Y.-f. Yang and D. Pines, Emergent states in heavy-electron materials, Proc. Natl Acad. Sci. USA **109**, E3060 (2012).

[23] V. Grinenko, P. Materne, R. Sarkar, H. Luetkens, K. Kihou, C. H. Lee, S. Akhmadaliev, D. V. Efremov, S.-L. Drechsler, and H.-H. Klauss, Superconductivity with broken time-reversal symmetry in ion-irradiated $Ba_{0.27}K_{0.73}Fe_2As_2$ single crystals, Phys. Rev. B **95**, 214511 (2017).

[24] S. Coh, M. L. Cohen, and S. G. Louie, Large electron–phonon interactions from FeSe phonons in a monolayer, New J. Phys. **17**, 073027 (2015).

[25] R. Lortz and C. H. Wong, Preliminary T_c calculations for iron-based superconductivity in NaFeAs, LiFeAs, FeSe and nanostructured $FeSe/SrTiO_3$ superconductors, Materials **16**, 4674 (2023).

[26] S. V. Borisenko, D. V. Evtushinsky, Z.-H. Liu, I. Morozov, R. Kappenberger, S. Wurmehl, B. Büchner, A. N. Yaresko, T. K. Kim, M. Hoesch, T. Wolf, and N. D. Zhigadlo, Direct observation of spin–orbit coupling in iron-based superconductors, Nat. Phys. **12**, 311 (2016).

[27] W. L. McMillian, Transition temperature of strong-coupled superconductors, Phys. Rev. **167**, 331 (1968).

[28] J. P. Perdew, J. A. Chevary, S. H. Vosko, K. A. Jackson, M. R. Pederson, D. J. Singh, and C. Fiolhais, Atoms, molecules, solids, and surfaces: Applications of the generalized gradient approximation for exchange and correlation, Phys. Rev. B **46**, 6671 (1992).

[29] See Supplemental Material at http://link.aps.org/supplemental/10.1103/PhysRevResearch.6.013121 for contains the raw data for the ab-initio calculations and also provide the demonstrations of the Tc calculations, which also contains Refs. [8,9,20,31,32,34,35].

[30] D. J. Kim, The influence of magnetism on the electron-phonon interaction in metals, Physica B+C **91**, 281 (1977).

[31] Y. Wen, D. Wu, R. Cao, L. Liu, and L. Song, The third-order elastic moduli and Debye temperature of $SrFe_2As_2$ and $BaFe_2As_2$: A first-principles study, J. Supercond. Nov. Magn. **30**, 1749 (2017).

[32] M. Rotter, M. Panger, M. Tegel, and D. Johrendt, Superconductivity and crystal structures of $(Ba_{1-x}K_x)Fe_2As_2$ $(x = 0 - 1)$, Angew. Chem. Int. Ed. **47**, 7949 (2008).

[33] H. Oh, S. Coh, and M. L. Cohen, Calculation of the specific heat of optimally K-doped $BaFe_2As_2$, J. Phys.: Condens. Matter **27**, 335504 (2015).

[34] R. Mittal, S. K. Mishra, S. L. Chaplot, S. V. Ovsyannikov, E. Greenberg, D. M. Trots, L. Dubrovinsky, Y. Su, Th. Brueckel, S. Matsuishi, H. Hosono, and G. Garbarino, Ambient- and low-temperature synchrotron x-ray diffraction study of $BaFe_2As_2$ and $CaFe_2As_2$ at high pressures up to 56 GPa, Phys. Rev. B **83**, 054503 (2011).

[35] J. R. Jeffries, N. P. Butch, K. Kirshenbaum, S. R. Saha, S. T. Weir, Y. K. Vohra, and J. Paglione, The suppression of magnetism and the development of superconductivity within the collapsed tetragonal phase of $Ca_{0.67}Sr_{0.33}Fe_2As_2$ at high pressure, Phys. Rev. B **85**, 184501 (2012).

[36] J.-Ph. Reid, M. A. Tanatar, A. Juneau-Fecteau, R. T. Gordon, S. René de Cotret, N. Doiron-Leyraud, T. Saito, H. Fukazawa, Y. Kohori, K. Kihou, C. H. Lee, A. Iyo, H. Eisaki, R. Prozorov, and L. Taillefer, Universal heat conduction in the iron arsenide superconductor KFe_2As_2: Evidence of a d-wave state, Phys. Rev. Lett. **109**, 087001 (2012).

[37] F. F. Tafti, A. Juneau-Fecteau, M.-È. Delage, S. René de Cotret, J.-Ph. Reid, A. F. Wang, X.-G. Luo, X. H. Chen, N. Doiron-Leyraud, and L. Taillefer, Sudden reversal in the pressure dependence of T_c in the iron-based superconductor KFe_2As_2, Nat. Phys. **9**, 349 (2013).

[38] A. Ptok, K. Rodríguez, and K. J. Kapcia, Superconducting monolayer deposited on substrate: Effects of the spin-orbit coupling induced by proximity effects, Phys. Rev. Mater. **2**, 024801 (2018).

[39] J. Hutchinson, J. E. Hirsch, and F. Marsiglio, Enhancement of superconducting T_c due to the spin-orbit interaction, Phys. Rev. B **97**, 184513. (2018).

[40] Q. Wang, L. Fanfarillo, and A. E. Böhmer, Nematicity in iron-based superconductors, Front. Phys. Condens. Matter Phys. **10**, 1 (2022).

[41] Y. Sato, S. Kasahara, T. Taniguchi, X. Xing, Y. Kasahara, Y. Tokiwa, Y. Yamakawa, H. Kontani, T. Shibauchi, and Y. Matsuda, Abrupt change of the superconducting gap structure at the nematic critical point in $FeSe_{1-x}S_x$, Proc. Natl Acad. Sci. USA **115**, 1227 (2018).

[42] J. Song and J. F. Annett, Electron-phonon coupling and d-wave superconductivity in the cuprates, Phys. Rev. B **51**, 3840 (1995).

[43] K.-C. Weng and C. D. Hu, The p-wave superconductivity in the presence of Rashba interaction in 2DEG, Sci. Rep. **6**, 29919 (2016).

[44] C. Tang, C. Liu, G. Zhou, F. Li, H. Ding, Z. Li, D. Zhang, Z. Li, C. Song, S. Ji, K. He, L. Wang, X. Ma, and Q.-K. Xue, Interface-enhanced electron-phonon coupling and high-temperature superconductivity in potassium-coated ultrathin FeSe films on $SrTiO_3$, Phys. Rev. B **93**, 020507(R) (2016).

[45] S. Zhang, J. Guan, Y. Wang, T. Berlijn, S. Johnston, X. Jia, B. Liu, Q. Zhu, Q. An, S. Xue *et al.*, Lattice dynamics of ultrathin FeSe films on $SrTiO_3$, Phys. Rev. B **97**, 035408 (2018).

[46] roywch654321@gmail.com.